

Origin of Quantum Criticality in Yb-Al-Au Approximant Crystal and Quasicrystal

Shinji Watanabe¹ and Kazumasa Miyake²

¹*Department of Basic Sciences, Kyushu Institute of Technology, Kitakyushu, Fukuoka 804-8550, Japan*

²*Toyota Physical and Chemical Research Institute, Nagakute, Aichi 480-1192, Japan*

To get insight into the mechanism of emergence of unconventional quantum criticality observed in quasicrystal $\text{Yb}_{15}\text{Al}_{34}\text{Au}_{51}$, the approximant crystal $\text{Yb}_{14}\text{Al}_{35}\text{Au}_{51}$ is analyzed theoretically. By constructing a minimal model for the approximant crystal, the heavy quasiparticle band is shown to emerge near the Fermi level because of strong correlation of 4f electrons at Yb. We find that charge-transfer mode between 4f electron at Yb on the 3rd shell and 3p electron at Al on the 4th shell in Tsai-type cluster is considerably enhanced with almost flat momentum dependence. The mode-coupling theory shows that magnetic as well as valence susceptibility exhibits $\chi \sim T^{-0.5}$ for zero-field limit and is expressed as a single scaling function of the ratio of temperature to magnetic field T/B over four decades even in the approximant crystal when some condition is satisfied by varying parameters, e.g., by applying pressure. The key origin is clarified to be due to the strong locality of the critical Yb-valence fluctuation and small Brillouin zone reflecting the large unit cell, giving rise to the extremely-small characteristic energy scale. This also gives a natural explanation for the quantum criticality in the quasicrystal corresponding to the infinite limit of the unit-cell size.

Recent discovery of unconventional quantum critical phenomena in quasicrystal $\text{Yb}_{15}\text{Al}_{34}\text{Au}_{51}$ has attracted much attention.^{1,2)} The measured criticality such as magnetic susceptibility $\chi \sim T^{-0.5}$, NMR relaxation rate $(T_1T)^{-1} \sim T^{-0.5}$, specific heat $C_e/T \sim -\log T$, and resistivity $\rho \sim T$ is unconventional and quite similar to those observed in periodic crystals such as heavy-electron metals YbRh_2Si_2 ³⁾ and $\beta\text{-YbAlB}_4$,^{4,5)} which are well explained by quantum critical phenomena of Yb-valence fluctuations.⁶⁾

The quasicrystal $\text{Yb}_{15}\text{Al}_{34}\text{Au}_{51}$ is constituted of concentric shell structures of Tsai-type cluster shown in Fig. 1.^{1,7)} There also exists approximant crystal $\text{Yb}_{14}\text{Al}_{35}\text{Au}_{51}$.⁷⁾ The approximant crystal has periodic arrangement of the body-centered cubic (bcc) structure whose unit cell contains shell structures shown in Figs. 1(a)-1(e). Theoretical analysis of the Yb-Al-Au cluster taking account of critical Yb-valence fluctuations has provided a natural explanation for robustness of quantum criticality in the quasicrystal measured under pressure and has pointed out a possibility that the same criticality appears even in the approximant crystal when pressure is applied.^{8,9)}

On the other hand, a new theoretical framework for critical Yb-valence fluctuation under magnetic field has been developed recently.¹⁰⁾ The theory has succeeded in explaining novel scaling discovered in $\beta\text{-YbAlB}_4$ where the magnetic susceptibility χ is expressed as a single scaling function of the ratio of temperature to magnetic field T/B over four decades.⁵⁾

Surprisingly, recent measurement of magnetic susceptibility in the quasicrystal $\text{Yb}_{15}\text{Al}_{34}\text{Au}_{51}$ has revealed that the same T/B -scaling behavior appears over six decades of T/B .¹¹⁾ This strongly suggests that the origin of both the unconventional criticality in the quasicrystal and periodic crystal $\beta\text{-YbAlB}_4$ is the same and calls for theoretical analysis from the viewpoint of the critical Yb-valence fluctuation.

Thus the aim of this Letter is to get insight into the origin of the unconventional criticality and the mechanism of emergence of the T/B scaling in the magnetic susceptibility observed in the quasicrystal from the viewpoint by perform-

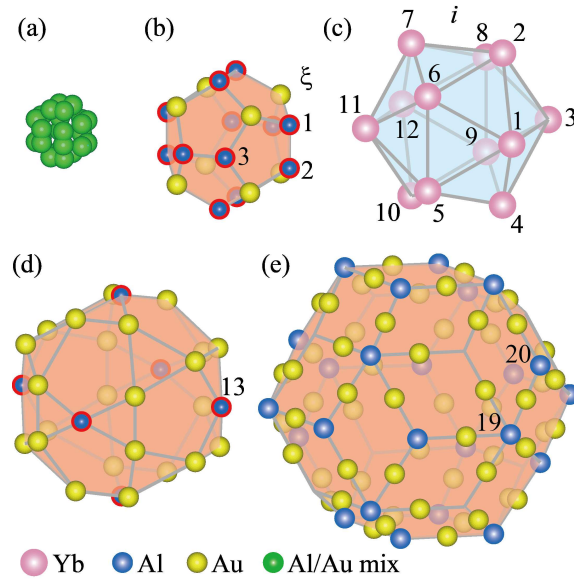


Fig. 1. (color online) Concentric shell structures of Tsai-type cluster in the Yb-Al-Au approximant: (a) first shell, (b) second shell, (c) third shell, (d) fourth shell, and (e) fifth shell. The number in (c) indicates the i -th Yb site and number in (b), (d), and (e) indicates the ξ -th Al site.

ing the explicit calculation. Since the locality of the critical Yb-valence fluctuation is considered to be the key origin, essentially the same phenomena are expected to occur in the approximant crystal when pressure is tuned.¹²⁾ Hence, we clarify the origin of the unconventional criticality and mechanism in the approximant crystal $\text{Yb}_{14}\text{Al}_{35}\text{Au}_{51}$.

Let us start with setting the model Hamiltonian. Recent measurement performed by replacing Al with Ga in the Yb-Al-Au quasicrystal has revealed that the quantum critical state disappears.¹³⁾ This suggests that the conduction electron at Al, presumably 3p electron, contributes to the quantum critical state. Hence, we consider the simplest minimal model for the 4f-hole orbital at the Yb site and the conduction-hole or-

bital at the Al site in the approximant crystal:

$$H = H_f + H_c + H_{\text{hyb}}. \quad (1)$$

The 4f-hole part is given by

$$H_f = \sum_{j=1}^{N_L} \left[\varepsilon_f \sum_{i=1\sigma}^{24} n_{ji\sigma}^f + U \sum_{i=1}^{24} n_{ji\uparrow}^f n_{ji\downarrow}^f \right], \quad (2)$$

where $f_{ji\sigma}^\dagger$ ($f_{ji\sigma}$) is the creation (annihilation) operator for f hole at the i -th site in the j -th unit cell with spin σ , and $n_{ji\sigma}^f \equiv f_{ji\sigma}^\dagger f_{ji\sigma}$. Here N_L is the number of unit cells and i specifies the Yb site on the Yb₁₂ cluster [see Fig. 1(c)] at the body center ($i = 1 \sim 12$) and at the 8 corners of the bcc unit cell ($i = 13 \sim 24$). The first term represents the f level and the 2nd term represents the on-site Coulomb repulsion of the 4f holes at the Yb sites.

The conduction-hole part is given by

$$H_c = - \sum_{\langle j\xi, j'\nu \rangle \sigma} \left(t_{j\xi, j'\nu} c_{j\xi\sigma}^\dagger c_{j'\nu\sigma} + \text{h.c.} \right), \quad (3)$$

where $c_{j\xi\sigma}^\dagger$ ($c_{j\xi\sigma}$) is the creation (annihilation) operator for conduction hole at the ξ -th site in the j -th unit cell with spin σ . Note that ξ specifies Al sites on the 2nd shell [see Fig. 1(b)] and the 4th shell [see Fig. 1(d)] at the body center and 8 corners at the unit cell (12×2 and 6×2 sites, respectively) and on the 5th shell [see Fig. 1(e)] (12 sites). Here $\langle j\xi, j'\nu \rangle$ denotes the pairs between the $j\xi$ -th Al site and the $j'\nu$ -th Al site. The transfer integrals $t_{j\xi, j'\nu}$ are set for the nearest-neighbor (N.N.) Al sites on the 2nd shell as t_2 and between the 2nd and 4th shells as t_{2-4} , and are set up to the next N.N. Al sites between the 4th and 5th shells as t_{4-5} . Since existence ratio of the 1st shell [see Fig. 1(a)] is quite small (Al/Au:7.8%/8.9%⁷), we consider the 2nd-5th shells. As a first step of analysis, here we consider the case that the Al/Au mixed sites framed in red in Fig. 1 are occupied by Al and degeneracy of the 3p orbital is neglected at Al sites. In reality, there may also exist conduction orbital at the Au site. To take into account this effect, we consider the effective transfer via the Au site as a parameter, which is expressed as t'_5 between the N.N. Al sites on the 5th shell since existence ratio of the Al's is 100%.⁷

The hybridization between 4f-hole and conduction-hole orbitals is given by

$$H_{\text{hyb}} = \sum_{\langle ji, j'\xi \rangle \sigma} \left(V_{ji, j'\xi} f_{ji\sigma}^\dagger c_{j'\xi\sigma} + \text{h.c.} \right), \quad (4)$$

where $\langle ji, j'\xi \rangle$ denotes the pairs between the ji -th site and the $j'\xi$ -th site and the hybridization matrix element is given by $V_{ji, j'\xi}$. Here i specifies the Yb site ($i = 1 \sim 24$) in the j -th unit cell and ξ specifies the N.N. Al sites on the 4th and 5th shells and up to the next N.N. Al sites on the 2nd shell in the j' -th unit cell for each i -th site. Corresponding $V_{ji, j'\xi}$ is expressed as V_{3-4} , V_{3-5} , and V_{2-3} , respectively.

To set transfer integrals, we employ the relation $t_{j\xi, j'\nu} \propto 1/r^{\ell+\ell'+1}$, where r is the distance between the $j\xi$ -th site and $j'\nu$ -th site with wave functions with azimuthal quantum numbers ℓ and ℓ' , respectively.¹⁴⁻¹⁶ By inputting $\ell = \ell' = 1$ and r obtained from Ref. 7, we have $t_{2-4} = 0.357t_2$ and t_{4-5} is set to be either of $0.173t_2$ or $0.052t_2$ corresponding to Al-Al distances (for instance, the former is set between the $\xi = 13$ th and 19th Al sites and the latter is set between the $\xi = 13$ th and 20th Al sites in Figs. 1(d) and 1(e), respectively). As for

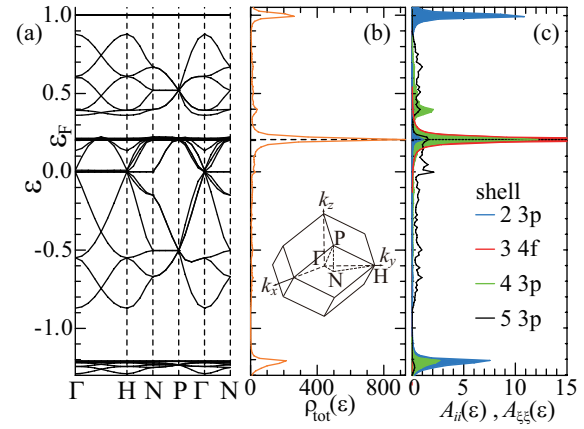


Fig. 2. (color online) (a) Energy band along high-symmetry lines for $t_2 = 1.0$, $t'_5 = 0.2$, $V_0 = 0.13$, $\varepsilon_f = -0.4$, and $U = \infty$ at $\bar{n} = 1$ calculated in $N_L = 8^3$. (b) Total density of states. Inset shows bcc Brillouin zone. (c) Spectral functions $A_{ii}(\varepsilon)$ for $i = 1$ (red) and $A_{\xi\xi}(\varepsilon)$ for $\xi = 1$ (blue), $\xi = 13$ (green), and $\xi = 19$ (black). Horizontal dashed lines indicate Fermi level ε_f .

the f-c hybridization, the similar relation $V_{ji, j'\xi} \propto 1/r^{\ell+\ell'+1}$ holds. Hence by inputting $\ell = 3$ and $\ell' = 1$ and the Yb-Al distance r , V_{3-4} and V_{3-5} are set as $V_{3-4} = 1.070V_0$ and $V_{3-5} = 0.714V_0$, respectively. V_{2-3} is set to be either of V_0 or $0.767V_0$ corresponding to Yb-Al distances (for instance, the former is set between the $i = 1$ st and $\xi = 1$ st sites and the latter is set between the $i = 1$ st and $\xi = 3$ rd sites in Figs. 1(c) and 1(b), respectively). Hereafter, the energy unit is taken as t_2 , i.e., $t_2 = 1.0$, and V_0 and t'_5 are set as parameters.

Heavy electron behavior observed in the approximant crystal Yb₁₄Al₃₅Au₅₁¹⁾ is considered to be originated from strong onsite Coulomb repulsion U between the 4f holes at Yb. To clarify the band structure for the heavy quasiparticles in the approximant crystal, we apply the slave-boson mean-field theory^{17,18)} for $U = \infty$ to Eq. (1). To describe the state for $U = \infty$, we consider $V_{ji, j'\xi} f_{ji\sigma}^\dagger b_i c_{j'\xi\sigma}$ instead of $V_{ji, j'\xi} f_{ji\sigma}^\dagger c_{j'\xi\sigma}$ by introducing the slave-boson operator b_i at the i -th site in the j -th unit cell to describe f^0 state and require the constraint $\sum_{\sigma} n_{ji\sigma}^f + b_i^\dagger b_i = 1$ with introducing the Lagrange multiplier λ_i , i.e., $\sum_i^{24} \lambda_i (\sum_{\sigma} n_{ji\sigma}^f + b_i^\dagger b_i - 1)$. We employ the mean-field treatment as $\bar{b}_i = \langle b_i \rangle$ and the resultant Hamiltonian is denoted by \tilde{H} . By optimizing the ground-state energy with respect to λ_i and \bar{b}_i , $\partial \langle \tilde{H} \rangle / \partial \lambda_i = 0$ and $\partial \langle \tilde{H} \rangle / \partial \bar{b}_i = 0$, the following mean-field equations are obtained:

$$\frac{1}{N_L} \sum_{\mathbf{k}\sigma} \langle f_{\mathbf{k}i\sigma}^\dagger f_{\mathbf{k}i\sigma} \rangle + \bar{b}_i^2 = 1, \quad (5)$$

$$\frac{1}{2N_L} \sum_{\mathbf{k}\sigma} \sum_{\xi} \left[V_{\mathbf{k}i\xi} \langle f_{\mathbf{k}i\sigma}^\dagger c_{\mathbf{k}\xi\sigma} \rangle + \text{h.c.} \right] + \lambda_i \bar{b}_i = 0, \quad (6)$$

for $i = 1, \dots, 24$.

The filling is defined by the hole number per site, which is given by $\bar{n} = \bar{n}_f + \bar{n}_c$ where $\bar{n}_f \equiv \frac{1}{N_L} \sum_{j=1}^{N_L} \frac{1}{24} \sum_{i=1}^{24} \sum_{\sigma} \langle n_{ji\sigma}^f \rangle$ and $\bar{n}_c \equiv \frac{1}{N_L} \sum_{j=1}^{N_L} \frac{1}{48} \sum_{\xi=1}^{48} \sum_{\sigma} \langle n_{j\xi\sigma}^c \rangle$ with $n_{j\xi\sigma}^c \equiv c_{j\xi\sigma}^\dagger c_{j\xi\sigma}$. We have solved Eqs. (5) and (6), and $\bar{n} = 1$ self-consistently at the ground state for several V_0 , ε_f , and t'_5 . Figure 2 shows the result for $V_0 = 0.13$, $\varepsilon_f = -0.4$ and $t'_5 = 0.2$ calculated in $N_L = 8 \times 8 \times 8$ as a typical case for the approximant crystal.

The renormalized f level is raised up to $\varepsilon \approx 0.2$, where

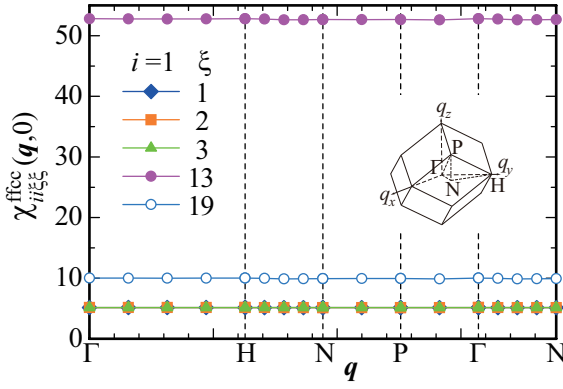


Fig. 3. (color online) $\chi_{ii\xi\xi,\sigma}^{\text{fcc}}(\mathbf{q}, 0)$ along high-symmetry lines for $i = 1$ and $\xi = 1$ (filled diamond), 2 (filled square), 3 (filled triangle), 13 (filled circle), and 19 (open circle) at $T = 0.0001$ calculated in $N_L = 8^3$ and $n_M = 2^{15}$ for $t_2 = 1.0$, $t'_5 = 0.2$, $V_0 = 0.13$, $\varepsilon_F = -0.4$, and $U = \infty$ at $\tilde{n} = 1$. Note that data for $\xi = 1$ and 2 are degenerated. Inset shows bcc Brillouin zone.

the Fermi level ε_F is located, giving rise to the heavy quasi-particle band in Fig. 2(a). This is reflected in the sharp peak of the total density of states (DOS) $\rho_{\text{tot}}(\varepsilon)$ around ε_F , so-called Kondo peak, in Fig. 2(b). Here, $\rho_{\text{tot}}(\varepsilon)$ is given by $\rho_{\text{tot}}(\varepsilon) = \rho_f(\varepsilon) + \rho_c(\varepsilon)$ with $\rho_f(\varepsilon) \equiv \sum_{i=1}^{24} A_{ii}^{\text{ff}}(\varepsilon)$ and $\rho_c(\varepsilon) \equiv \sum_{\xi=1}^{48} A_{\xi\xi}^{\text{cc}}(\varepsilon)$, where spectral function $A_{bb}^{\text{aa}}(\varepsilon)$ is defined as $A_{bb}^{\text{aa}}(\varepsilon) \equiv -\frac{1}{\pi N_L} \sum_{\mathbf{k}} \text{Im} G_{bb}^{\text{aa}R}(\mathbf{k}, \varepsilon)$ with the retarded Green function for quasiparticles $G^R(\mathbf{k}, \varepsilon) \equiv (\varepsilon + i\delta - \tilde{H}_{\mathbf{k}})^{-1}$ and $\delta = 0.01$. Here, $\tilde{H}_{\mathbf{k}}$ is given by $\tilde{H} = \sum_{\mathbf{k}} \tilde{H}_{\mathbf{k}}$. Since ε_F is located at rather deep position from the Fermi level, the present state is considered to correspond to pressurized approximant crystal. Actually, at the Fermi level, the f-component is dominant with $\rho_f(\varepsilon_F)$ being sharing 79.5% of $\rho_{\text{tot}}(\varepsilon_F)$. The conduction bands of 3p holes on the 4th, 2nd, and 5th shells hybridize with 4f holes with each DOS at ε_F sharing 15.7%, 2.8%, and 2.0% of $\rho_{\text{tot}}(\varepsilon_F)$, respectively, forming three hybridized bands at ε_F below pseudo-gap-like DOS around $\varepsilon \sim 0.3$ in Fig. 2(b). Almost flat dispersions around $\varepsilon \approx -1.2$ and 1.0 in Fig. 2(a) are reflected in marked DOS's in Fig. 2(b), respectively, which are mainly due to splitting of 3p bands on the 2nd shell [see Fig. 2(c)].

The dynamical susceptibility for the charge transfer between 4f and conduction holes

$$\chi_{ii\xi\xi,\sigma}^{\text{fcc}}(\mathbf{q}, i\omega_m) = -\frac{T}{N_L} \sum_{n\mathbf{k}} G_{ii,\sigma}^{\text{ff}}(\mathbf{k} + \mathbf{q}, i\varepsilon_n + i\omega_m) G_{\xi\xi,\sigma}^{\text{cc}}(\mathbf{k}, i\varepsilon_n) \quad (7)$$

is calculated by using $G(\mathbf{k}, i\varepsilon_n) \equiv (i\varepsilon_n - \tilde{H}_{\mathbf{k}} + \mu)^{-1}$ with $\varepsilon_n = (2n+1)\pi T$ and the chemical potential μ , and $\omega_m = 2m\pi T$. The \mathbf{q} dependence of $\chi_{ii\xi\xi,\sigma}^{\text{fcc}}(\mathbf{q}, 0)$ calculated at $T = 0.0001$ with the number of Matsubara frequency $n_M = 2^{15}$ being kept is shown in Fig. 3. A remarkable result is that almost flat-momentum dependence appears in the charge-transfer mode between the $i = 1$ st Yb site [see Fig. 1(c)] and the $\xi = 1$ st, 2nd, 3rd Al sites [see Fig. 1(b)], $\xi = 13$ th Al site [see Fig. 1(d)], and $\xi = 19$ th Al site [see Fig. 1(e)], which are connected via H_{hyb} in Eq. (4). Emergence of almost flat mode is considered to be ascribed to strong local correlation effect by $U = \infty$.^{6, 19, 20)}

The reason why the charge-transfer mode between the 3rd and 4th shells is extraordinary enhanced [see the $(i, \xi) = (1, 13)$ data in Fig. 3] is due to the strongest f-c hybridization, $|V_{3-4}| > |V_{2-3}|, |V_{3-5}|$, arising from the shortest Yb-Al

distance and existence of the DOS around ε_F [see $A_{\xi\xi}^{\text{cc}}(\varepsilon_F)$ for $\xi = 13$ in Fig. 2(c)]. Maximum of $\chi_{ii\xi\xi,\sigma}^{\text{fcc}}(\mathbf{q}, 0)$ for $i = 1$ and $\xi = 13$ is located at the Γ point, $\mathbf{q} = \mathbf{0}$.

To clarify how the locality of the charge-transfer fluctuation affects the quantum criticality, and also to get insight into the mechanism of emergence of the T/B scaling, let us focus on the charge-transfer mode between the N.N. Yb on the 3rd shell and Al on the 4th shell since it is overwhelmingly dominant in Fig. 3 [see the $(i, \xi) = (1, 13)$ data]. Then, we apply the recently-developed mode-coupling theory for critical valence fluctuations under magnetic field¹⁰⁾ to the present system, which starts from the Hamiltonian

$$\mathcal{H} = H + H_{U_{\text{fc}}} + H_{\text{Zeeman}}, \quad (8)$$

where the charge-transfer fluctuation, i.e., Yb-valence fluctuation, is caused by the inter-orbital Coulomb repulsion^{6, 18, 19)}

$$H_{U_{\text{fc}}} = U_{\text{fc}} \sum_{\langle ji, j'\xi \rangle \sigma \sigma'} n_{ji\sigma}^f n_{j'\xi\sigma'}^c. \quad (9)$$

Here, $\langle ji, j'\xi \rangle$ denotes the N.N. pair between Yb on the 3rd shell and Al on the 4th shell. The Zeeman term is given by

$$H_{\text{Zeeman}} = -h \sum_{j=1}^{N_L} \left[\sum_{i=1}^{24} S_{ji}^{fz} + \sum_{\xi=1}^{48} S_{j\xi}^{cz} \right], \quad (10)$$

where h is magnetic field, and $S_{ji}^{fz} \equiv \frac{1}{2}(n_{ji\uparrow}^f - n_{ji\downarrow}^f)$ and $S_{j\xi}^{cz} \equiv \frac{1}{2}(n_{j\xi\uparrow}^c - n_{j\xi\downarrow}^c)$.

Taking into account the mode-coupling effects of the charge-transfer fluctuation up to the 4th order of U_{fc} in the action $S[\varphi]$ for \mathcal{H} , which is derived by introducing the Stratonovich-Hubbard transformation for $H_{U_{\text{fc}}}$ (see Ref. 10 for detail), we construct the action for the Gaussian fixed point. By using Feynman's inequality,²¹⁾ the free energy for \mathcal{H} is evaluated as $F \leq F_{\text{eff}} + T\langle S - S_{\text{eff}} \rangle_{\text{eff}} \equiv \tilde{F}(\eta)$, where S_{eff} is the effective action for the best Gaussian, $S_{\text{eff}}[\varphi] = \frac{1}{2} \sum_{\sigma} \sum_{\mathbf{q}, m} \chi_{\nu\sigma}(\mathbf{q}, i\omega_m)^{-1} |\varphi_{\sigma}(\mathbf{q}, i\omega_m)|^2$. Here, the valence susceptibility $\chi_{\nu\sigma}(\mathbf{q}, i\omega_m)$ is defined as

$$\chi_{\nu\sigma}(\mathbf{q}, i\omega_m)^{-1} \approx \eta + A_{\sigma} q^2 + C_{\sigma} \frac{|\omega_m|}{q}. \quad (11)$$

and F_{eff} is the free energy for the best Gaussian. By optimizing $\tilde{F}(\eta)$ by η , $\frac{d\tilde{F}(\eta)}{d\eta} = 0$, the mode-coupling equation under magnetic field is derived in the $A_{\sigma} q_{B\sigma}^2 \lesssim \eta$ region as

$$\begin{aligned} & \sum_{\sigma} A_{\sigma} q_{B\sigma}^4 \frac{T_{0\sigma}}{T_{A\sigma}^2} \left(1 + \frac{v_{4\sigma} q_{B\sigma}^3 T_{0\sigma}}{\pi^2 T_{A\sigma}^2} \right) \\ & \times \left[y_{0\sigma} - \tilde{y}_{\sigma} + \frac{3}{2} y_{1\sigma} t_{\sigma} \left\{ \frac{x_c^3}{6\tilde{y}_{\sigma}} - \frac{1}{2\tilde{y}_{\sigma}} \int_0^{x_c} \frac{x^3}{x + \frac{t_{\sigma}}{6\tilde{y}_{\sigma}}} dx \right\} \right] \\ & \times \left[C_{2\sigma} + \frac{t_{\sigma} x_c^3}{3\tilde{y}_{\sigma}^2} - \frac{t_{\sigma}}{\tilde{y}_{\sigma}^2} \int_0^{x_c} \frac{x^4}{\left(x + \frac{t_{\sigma}}{6\tilde{y}_{\sigma}}\right)^2} dx \right] = 0, \quad (12) \end{aligned}$$

where $\tilde{y}_{\sigma} = y \frac{A_{\sigma}}{A_{\sigma'}} \left(\frac{q_B}{q_{B\sigma}} \right)^2$, $t_{\sigma} = \frac{T}{T_{0\sigma}}$, $T_{0\sigma} = \frac{A_{\sigma} q_{B\sigma}^3}{2\pi C_{\sigma}}$, and $T_{A\sigma} = \frac{A_{\sigma} q_{B\sigma}^2}{2}$ with $q_{B\sigma}$ being the Brillouin zone. Here, y is defined as $y \equiv \frac{\eta}{A_{\sigma}^2}$, and the dimensionless variable and its cutoff are defined as $x \equiv q/q_B$ and $x_c \equiv q_c/q_B$, respectively. Note that A , C , and q_B are the zero-field values of A_{σ} , C_{σ} , and $q_{B\sigma}$,

respectively. The parameters $y_{0\sigma}$ and $y_{1\sigma}$ are given by

$$y_{0\sigma} = \frac{\frac{\eta_{0\sigma}}{A_\sigma q_{B\sigma}^2} + v_{4\sigma} \frac{T_{0\sigma}}{T^2} \frac{q_{B\sigma}^3}{\pi^2} C_{1\sigma}}{1 + v_{4\sigma} \frac{T_{0\sigma}}{T^2} \frac{q_{B\sigma}^3}{\pi^2} C_{2\sigma}}, \quad (13)$$

$$y_{1\sigma} = \frac{v_{4\sigma} \frac{T_{0\sigma}}{T^2} \frac{4q_{B\sigma}^3}{3\pi^2}}{1 + v_{4\sigma} \frac{T_{0\sigma}}{T^2} \frac{q_{B\sigma}^3}{\pi^2} C_{2\sigma}}, \quad (14)$$

respectively, where $\eta_{0\sigma}$ is defined as $\eta_{0\sigma} \equiv U_{fc} [1 - U_{fc} \chi_{ii\xi\xi}^{\text{fcc}}(\mathbf{0}, 0)]$ and the mode-coupling constant of the 4th order $v_{4\sigma}$ is calculated as

$$v_{4\sigma} = \frac{U_{fc}}{4} \left[\frac{T}{2N_L} \sum_n \sum_{\mathbf{k}} G_{\xi\xi,\sigma}^{\text{cc}}(\mathbf{k}, i\varepsilon_n)^2 G_{ii,\sigma}^{\text{ff}}(\mathbf{k}, i\varepsilon_n)^2 + \frac{T}{N_L} \sum_n \sum_{\mathbf{k}} G_{\xi i,\sigma}^{\text{cf}}(\mathbf{k}, i\varepsilon_n) G_{ii,\sigma}^{\text{ff}}(\mathbf{k}, i\varepsilon_n) G_{i\xi,\sigma}^{\text{fc}}(\mathbf{k}, i\varepsilon_n) G_{\xi\xi,\sigma}^{\text{cc}}(\mathbf{k}, i\varepsilon_n) \right].$$

The constants $C_{1\sigma}$ and $C_{2\sigma}$ are given by

$$C_{1\sigma} = \int_0^{x_c} dx x^3 \ln \left| \frac{(A_\sigma q_{B\sigma}^2 x^3)^2 + (C_\sigma \omega_c / q_{B\sigma})^2}{(A_\sigma q_{B\sigma}^2 x^3)^2} \right| \text{ and } C_{2\sigma} = 2(C_\sigma \omega_c)^2 \int_0^{x_c} dx \frac{x}{(A_\sigma q_{B\sigma}^2 x^3)^2 + (C_\sigma \omega_c)^2}, \text{ respectively.}$$

To proceed the calculation in Fig. 3 to the mode-coupling theory for the approximant crystal, here we try to estimate the momentum and frequency dependence of $\chi_{ii\xi\xi}^{\text{fcc}}(\mathbf{q}, i\omega_m)$ in the vicinity of $\chi_{ii\xi\xi}^{\text{fcc}}(\mathbf{0}, 0)$, as follows:

The \mathbf{q}^2 -coefficient is evaluated as

$$\chi_{ii\xi\xi,\sigma}^{\text{fcc}}(\mathbf{q}_v, 0) = \chi_{ii\xi\xi,\sigma}^{\text{fcc}}(\mathbf{0}, 0) - A_{v,\sigma} \mathbf{q}_v^2, \quad (16)$$

where $\mathbf{q}_v = \frac{2\pi}{a}(\frac{2}{N_1}, 0, 0)$, $\frac{2\pi}{a}(0, \frac{2}{N_2}, 0)$, $\frac{2\pi}{a}(0, 0, \frac{2}{N_3})$, $\frac{2\pi}{a}(\frac{1}{N_1}, \frac{1}{N_2}, 0)$, $\frac{2\pi}{a}(0, \frac{1}{N_2}, \frac{1}{N_3})$, $\frac{2\pi}{a}(\frac{1}{N_1}, 0, \frac{1}{N_3})$ with $a = 14.5 \text{ \AA}$ being a lattice constant in the $N_L = N_1 N_2 N_3$ system. Then, we evaluate A_σ in Eq. (11) as $A_\sigma \approx U_{fc}^2 A_{av,\sigma}$ by employing the averaged value $A_{av,\sigma} = \frac{1}{6} \sum_{v=1}^6 A_{v,\sigma}$.

As for the frequency dependence,

$$\chi_{ii\xi\xi,\sigma}^{\text{fcc}}(\mathbf{q}_v, i\omega_1) - \chi_{ii\xi\xi,\sigma}^{\text{fcc}}(\mathbf{q}_v, 0) \approx -C_{v,\sigma} \frac{|\omega_1|}{q_v}, \quad (17)$$

where $q_v = |\mathbf{q}_v|$ and here inter-band contribution is neglected since intra-band contribution is dominant. Then, we evaluate C_σ in Eq. (11) as $C_\sigma \approx U_{fc}^2 C_{av,\sigma}$ by employing the averaged value $C_{av,\sigma} = \frac{1}{6} \sum_{v=1}^6 C_{v,\sigma}$.

In this way, the mode-coupling theory can be applied to the approximant crystal. The procedure of the calculation is as follows: First, we solve the slave-boson mean-field equations [Eqs. (5) and (6)] at $T = 0$ for a given set of parameters: t_2 , t_5' , V_0 , ε_f , $U = \infty$, and h at filling \bar{n} . Second, we calculate $\chi_{ii\xi\xi,\sigma}^{\text{fcc}}(\mathbf{q}, i\omega_m)$ in Eq. (7) and the [...] part in Eq. (15) by using the mean-field solution. Then, we obtain $\eta_{0\sigma}$ and $v_{4\sigma}$ for a given U_{fc} . Third, by using $y_{0\sigma}$ and $y_{1\sigma}$ obtained from Eqs. (13) and (14), respectively, we solve the mode-coupling equation [Eq. (12)] for critical valence fluctuations and finally obtain the solution $y(T)$.

At the QCP of valence transition, the magnetic susceptibility χ as well as the valence susceptibility $\chi_v(\mathbf{0}, 0)$ diverges with the same singularity, $\chi \propto \chi_v(\mathbf{0}, 0) \propto y^{-1}$, since the many body effect for U_{fc} common to both χ and $\chi_v(\mathbf{0}, 0)$ is enhanced near the QCP.⁶⁾

By setting the parameters used in Fig. 3, we perform the

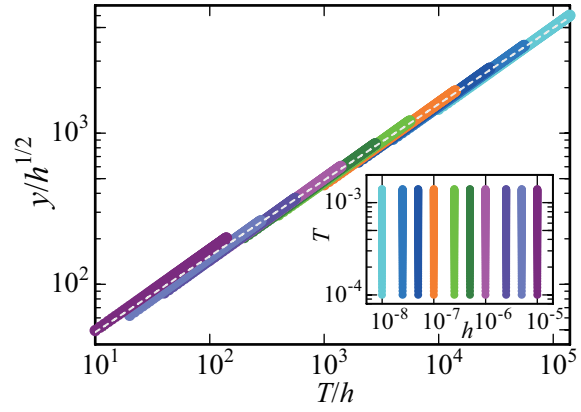


Fig. 4. (color online) Scaling of the data for $0.0001 \leq T \leq 0.0014$ and $10^{-8} \leq h \leq 10^{-5}$. Inset shows the T - h range where the scaling applies. The dashed line represents the fitting function $c(T/h)^\zeta$ with $\zeta = 0.503$. The data were obtained for $t_2 = 1.0$, $t_5' = 0.2$, $V_0 = 0.13$, $\varepsilon_f = -0.4$, $U_{fc} = 0.0192$, and $U = \infty$ at $\bar{n} = 1$ in $N_L = 8^3$ and $n_M = 2^{15}$. (15)

above procedure. Here we calculate $\chi_{ii\xi\xi}^{\text{fcc}}(\mathbf{q}, i\omega_m)$ and $v_{4\sigma}$ at $T = 0.0001$ with μ being determined so as to satisfy $\bar{n} = 1$ and temperature evolution of $y(T)$ is obtained by solving Eq. (12). Since approximant crystal has large unit cell with $a = 14.5 \text{ \AA}$, $q_B = \frac{2\pi}{a}$ is one-order of magnitude smaller than those of usual periodic crystals. This makes characteristic temperature of critical valence fluctuation $T_0 \equiv \frac{Aq_B^3}{2\pi C}$ reduced. Indeed we obtained $T_0 = 1.4 \times 10^{-4}$, which is four-order of magnitude smaller than the band width (see Fig. 2). The QCP of valence transition is identified as $U_{fc} = 0.0192$ where $y(0)$ becomes zero.

Figure 4 shows the result of the solution of Eq. (12) for $0.0001 \leq T \leq 0.0014$ and $10^{-8} \leq h \leq 10^{-5}$ at the QCP. We find that the data seem to fall down to a single scaling function of T/h over four decades.

$$y = h^{1/2} \phi\left(\frac{T}{h}\right). \quad (18)$$

The least-square fit for the large T/h regime of $10^2 \leq T/h \leq 1.4 \times 10^5$ gives $\frac{y}{h} = c \left(\frac{T}{h}\right)^\zeta$ with $\zeta = 0.503$, which is shown as a dashed line. This indicates that scaling function for $x \gg 1$ has the form of $\phi(x) = cx^{1/2}$. In this $T/h \gg 1$ region, we have $y/h^{1/2} \approx c(T/h)^{1/2}$, i.e., $y \approx T^{1/2}$. This is caused by critical valence fluctuation with strong locality, giving rise to the non-Fermi-liquid regime. This result indicates that the magnetic susceptibility behaves as $\chi \approx T^{-1/2}$ for $h \rightarrow 0$, which has been observed in quasicrystal $\text{Yb}_{15}\text{Al}_{34}\text{Au}_{51}$.¹⁾ Our result implies that even in the approximant crystal, the same behavior is expected to appear when pressure is applied.

As T/h decreases, the data tend to show deviation from the dashed line as seen in Fig. 4. This reflects suppression of valence susceptibility by magnetic field and indicates crossover to the Fermi liquid regime toward $T/h \ll 1$.

Emergence of the T/h scaling behavior is ascribed to presence of small characteristic temperature of critical valence fluctuation T_0 . In case that T_0 is below (or at least comparable to) the lowest temperature, $t/y \gg 1$ holds where all the terms with y and t in Eq. (12) can be expressed as scaling forms of $y/h^{1/2}$ and t/h , respectively.¹⁰⁾ We have confirmed that this is the case for all the data used in Fig. 4. Hence, real-

ization of small T_0 coming from almost flat- \mathbf{q} charge-transfer mode (see Fig. 3) assisted by small Brillouin zone q_B reflecting large unit cell is the main reason for emergence of the T/h scaling as well as $\chi \sim T^{-1/2}$ for the zero-field limit.

In reality, there exist $3p_x$, $3p_y$, $3p_z$ bands from Al and $6s$ band from Au. Those conduction bands are folded into small Brillouin zone and hybridizations between them each other give rise to many splits into bonding and antibonding bands.²²⁾ Hence, conduction bands themselves have the flat- \mathbf{q} nature. Hybridization between f and their bands is expected to further promote locality of valence fluctuations.

On the basis of the solution obtained in Eq. (12), it is shown that critical Yb-valence fluctuation causes a new type of criticality such as NMR relaxation rate $(T_1T)^{-1} \propto \chi \sim T^{-0.5}$, specific heat $C_e/T \sim -\log T$, and T -linear resistivity for $T/T_0 \gtrsim 1$.^{6,10)} Applying pressure to the approximant crystal is considered to make the f -hole level decrease and U_{fc} increase. Hence, the quantum valence criticality is expected to appear under pressure. The quasicrystal corresponds to the infinite limit of the unit-cell size in the approximant crystal. Then, the quasicrystal is regarded as the system with the small limit of the Brillouin zone, $q_B \rightarrow 0$, giving rise to vanishing characteristic temperature of critical Yb-valence fluctuation, i.e., $T_0 \equiv \frac{Aq_B^3}{2\pi C} \rightarrow 0$. Hence, T_0 is expected to be smaller than the measured lowest temperature, so that present mechanism is considered to capture the essence of the origin of the unconventional critical phenomena as above including the T/B scaling in χ observed in $\text{Yb}_{15}\text{Al}_{34}\text{Au}_{51}$.

Acknowledgements We thank N. K. Sato, K. Deguchi, S. Matsukawa, T. Ishimasa, and T. Watanuki for showing us experimental data with enlightening discussions on their analyses. This work was supported by Grants-in-Aid for Scientific Research (No. 24540378, No. 25400369 and No. 16H01077A01) from the Japan Society for the Promotion of Science (JSPS).

- 1) K. Deguchi, S. Matsukawa, N. K. Sato, T. Hattori, K. Ishida, H. Takakura, and T. Ishimasa, *Nature Mat.* **11**, 1013 (2012).
- 2) T. Watanuki, S. Kashimoto, D. Kawana, T. Yamazaki, A. Machida, Y. Tanaka, and T. J. Sato, *Phys. Rev. B* **86**, 094201 (2012).
- 3) P. Gegenwart, J. Custers, Y. Tokiwa, C. Geibel, and F. Steglich, *Phys. Rev. Lett.* **94**, 076402 (2005).
- 4) S. Nakatsuji, K. Kuga, Y. Machida, T. Tayama, T. Sakakibara, Y. Karaki, H. Ishimoto, S. Yonezawa, Y. Maeno, E. Pearson, G. G. Lonzarich, L. Balicas, H. Lee, and Z. Fisk, *Nat. Phys.* **4**, 603 (2008).
- 5) Y. Matsumoto, S. Nakatsuji, K. Kuga, Y. Karaki, N. Horie, Y. Shimura, T. Sakakibara, A. H. Nevidomskyy, and P. Coleman, *Science* **331**, 316 (2011).
- 6) S. Watanabe and K. Miyake, *Phys. Rev. Lett.* **105**, 186403 (2010).
- 7) T. Ishimasa, Y. Tanaka, and S. Kashimoto, *Phil. Mag.* **91**, 4218 (2011).
- 8) S. Watanabe and K. Miyake, *J. Phys. Soc. Jpn.* **82**, 083704 (2013).
- 9) S. Watanabe and K. Miyake, *J. Phys.: Conf. Ser.* **592**, 012087 (2015).
- 10) S. Watanabe and K. Miyake, *J. Phys. Soc. Jpn.* **83**, 103708 (2014).
- 11) K. Deguchi and N. K. Sato, private communications.
- 12) Just before submitting the present paper, we have been aware of the experimental fact that essentially the same behavior was observed in the approximant crystal under pressure: S. Matsukawa, K. Deguchi, K. Imura, T. Ishimasa, and N. K. Sato, submitted.
- 13) S. Matsukawa, K. Tanaka, M. Nakayama, K. Deguchi, K. Imura, H. Takakura, S. Kashimoto, T. Ishimasa, and N. K. Sato, *J. Phys. Soc. Jpn.* **83**, 034705 (2014).
- 14) O. K. Andersen and O. Jepsen, *Physica B* **91**, 317 (1977).
- 15) O. K. Andersen, W. Klose, and H. Nohl, *Phys. Rev. B* **17**, 1209 (1978).
- 16) W. A. Harrison, *Electronic Structure and the Properties of Solids* (W. H. Freeman and Co., San Francisco, 1980).
- 17) N. Read and D. M. Newns, *J. Phys. C: Solid State Phys.* **16**, 3273 (1983).
- 18) Y. Onishi and K. Miyake, *J. Phys. Soc. Jpn.* **69**, 3955 (2000).
- 19) K. Miyake, *J. Phys.: Condens. Matter* **19**, 125201 (2007).
- 20) S. Watanabe and K. Miyake, *J. Phys.: Condens. Matter* **24**, 294208 (2012).
- 21) R. P. Feynman, *Statistical Mechanics* (Addison-Wesley, Reading, Massachusetts, 1990) Sect. 3.4.
- 22) T. Fujiwara, *Phys. Rev. B* **40**, 942 (1989).